

Metaplasticity-Enabled Graphene Quantum Dot Devices for Mitigating Catastrophic Forgetting in Artificial Neural Networks

Xuemeng Fan, Anzhe Chen, Zongwen Li, Zhihao Gong, Zijian Wang, Guobin Zhang, Pengtao Li, Yang Xu, Hua Wang, Changhong Wang,* Xiaolei Zhu,* Rong Zhao, Bin Yu, and Yishu Zhang*

The limitations of deep neural networks in continuous learning stem from oversimplifying the complexities of biological neural circuits, often neglecting the dynamic balance between memory stability and learning plasticity. In this study, artificial synaptic devices enhanced with graphene quantum dots (GQDs) that exhibit metaplasticity is introduced, a higher-order form of synaptic plasticity that facilitates the dynamic regulation of memory and learning processes similar to those observed in biological systems. The GQDs-assisted devices utilize interface-mediated modifications in asymmetric conductive pathways, replicating classical synaptic plasticity mechanisms. This allows for repeatable and linearly programmable adjustments to future weight changes linked to historical weights. Incorporating metaplasticity is essential for achieving generalization within deep neural networks, which enables them to adapt more fluidly to new information while retaining previously acquired knowledge. The GQDs-device-based system achieved a 97% accuracy on the fourth MNIST dataset task, while consistently achieving performance levels above 94% on prior tasks. This performance substantiates the feasibility of directly transferring metaplasticity principles to deep neural networks, thereby addressing the challenges associated with catastrophic forgetting. These findings present a promising hardware solution for developing neuromorphic systems with robust and sustained learning capabilities that can effectively bridge the gap between artificial and biological neural networks.

1. Introduction

Deep neural networks have exhibited remarkable advancements across various fields, including game playing,^[1] computer vision tasks,^[2] and natural language processing,^[3] often surpassing human-level performance in select domains. However, these advancements rely on the premise of overwriting historical knowledge to acquire new skills—a phenomenon known as catastrophic forgetting.^[4] Catastrophic forgetting poses a significant challenge for numerous neural network architectures, including convolutional neural networks (CNNs) and recurrent neural networks (RNNs).^[5,6] In stark contrast, biological brains have developed the capability for lifelong continuous learning, facilitated by mechanisms that promote both plasticity for acquiring new information and stability for consolidating prior knowledge.^[7] The task of reconciling the catastrophic forgetting characteristic of artificial neural networks with the continuous learning abilities of biological systems introduces a synaptic plasticity–stability dilemma that remains an unresolved challenge in the

X. Fan, A. Chen, Z. Li, Z. Wang, G. Zhang, P. Li, Y. Xu, H. Wang, X. Zhu, B. Yu, Y. Zhang
 School of Integrated Circuits
 Zhejiang University
 Hangzhou, Zhejiang 311200, China
 E-mail: xl_zhu@zju.edu.cn; zhangyishu@zju.edu.cn
 X. Fan, A. Chen, Z. Li, Z. Gong, Z. Wang, G. Zhang, P. Li, Y. Xu, H. Wang, X. Zhu, B. Yu, Y. Zhang
 ZJU-Hangzhou Global Scientific and Technological Innovation Center
 Hangzhou, Zhejiang 310027, China

C. Wang
 Eastern Institute for Advanced Study
 Eastern Institute of Technology
 Ningbo 315200, China
 E-mail: cwang@eitech.edu.cn
 R. Zhao
 Department of Precision Instruments
 Tsinghua University
 Beijing 100084, China



The ORCID identification number(s) for the author(s) of this article can be found under <https://doi.org/10.1002/adma.202411237>

DOI: 10.1002/adma.202411237

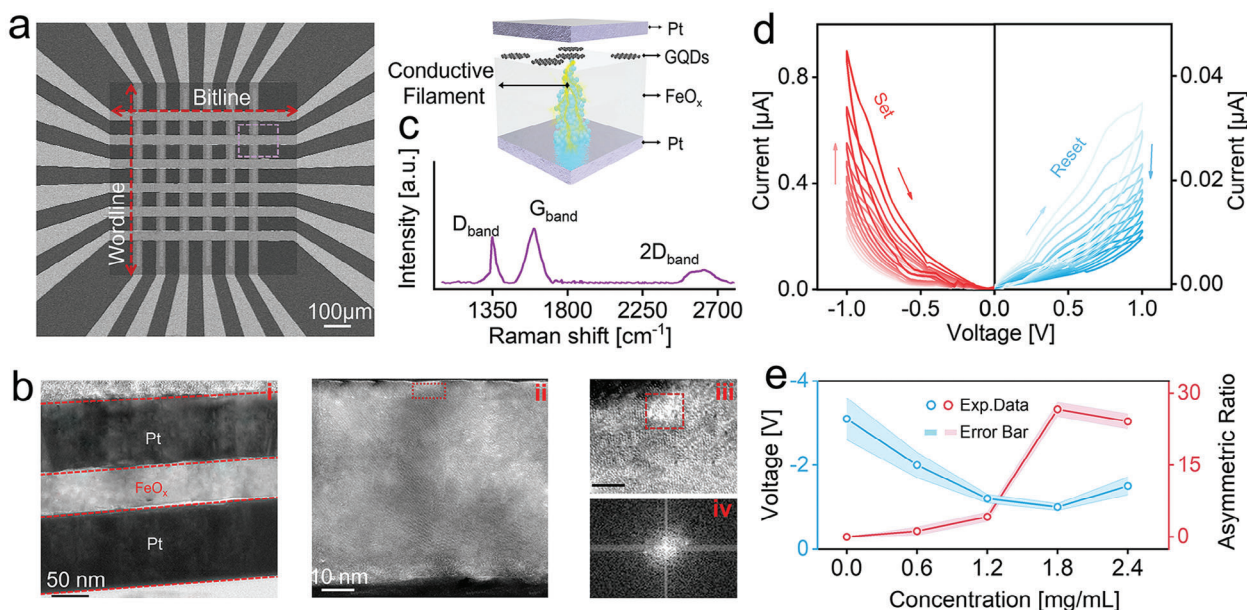


Figure 1. a) Schematic of the crossbar memory array and memristor structure. b) Cross-sectional HR-TEM image of i) device, ii) zoom-in FeO_x area, iii) corresponding HR-TEM image of GQDs, and iv) corresponding fast Fourier transform scattering pattern (FFT) image of GQDs. c) Raman spectrum of GQDs. d) Analog current–voltage (*I*–*V*) curves under 10 consecutive positive sweeps (0 to 1 V) and 10 consecutive negative sweeps (0 to –1 V), concentrations of GQDs: 1.8 mg mL^{–1}. e) Curves of asymmetric ratio and switch voltage varying at different GQDs concentrations.

field. As the scale and complexity of datasets and tasks continue to expand, addressing the issue of catastrophic forgetting is essential for advancing artificial intelligence.^[8]

Synaptic plasticity is a fundamental process that enables the biological brain to learn and adapt continuously through experiences. Metaplasticity refers to a higher-order form of synaptic modification described as the plasticity of plasticity, which enhances memory retention while permitting further plastic changes.^[9] The development of artificial synapses that emulate the mechanisms of biological plasticity is vital for the advancement of neuromorphic computing. The quintessential form of synaptic plasticity observed in biological systems is spike-timing-dependent plasticity (STDP), which has been experimentally validated in artificial synapses.^[10] Additionally, short-term plasticity (STP) temporarily alters synaptic efficacy via rapid decay, whereas long-term potentiation (LTP) induces enduring changes following repeated stimulation.^[11,12] Although various material systems have been explored to realize plasticity behaviors, only a few have achieved synaptic metaplasticity which is critical for overcoming catastrophic forgetting in neural networks.^[13–15] Recent advancements have been made in achieving continuous programmable conductance modulation through metaplasticity utilizing graphene transistors.^[16] However, the existing incompatibility between material transfer techniques and scalable manufacturing presents significant obstacles to the realization of effective neural network hardware. To overcome this challenge, innovative materials and device architectures require exploration to facilitate the development of scalable and reconfigurable neural network hardware capable of direct integration with metaplasticity.^[17,18]

In this study, we present a novel two-terminal metaplastic resistive memory device constructed from GQDs and iron oxide

(FeO_x). This device is designed to promote the development of scalable neural network hardware tailored for continual learning applications. The GQDs-assisted configuration enables interface-mediated alterations of asymmetric conduction pathways for plasticity and conductance regulation. This enhancement enriches the synaptic operations within artificial neural networks. By employing a variety of pulse amplitude programming techniques, these GQDs-assisted synaptic devices demonstrate a continual learning capability that parallels the dynamic regulation of memory and learning observed in the biological hippocampus. To assess the efficacy of the GQDs-based system in addressing the issue of catastrophic forgetting, we utilized established neural network architectures for continuous recognition learning across four distinct MNIST datasets. Remarkably, the system attained an accuracy of 97% on the fourth task while consistently maintaining performance levels above 94% on preceding tasks. This outcome underscores the potential of this approach as a robust solution to the challenges associated with catastrophic forgetting. By leveraging GQDs-assisted synaptic devices, we construct an adaptive neural network capable of responding to dynamic environments through the modulation of metaplasticity weights, thereby achieving both stability and continuous learning.

2. Results and Discussion

2.1. Device Structure and Electrical Behaviors

The metaplastic devices are composed of a resistive FeO_x layer sandwiched between platinum (Pt) electrodes, with GQDs that modulate the conductive pathway. Comprehensive details regarding the device fabrication and characterization methodologies are

presented in the Experimental Section (Figure S1, Supporting Information). To assess the feasibility of developing neural network hardware layers, a 6×6 array was constructed (Figure 1a). High-resolution transmission electron microscopy (HR-TEM) provides insight into the structural properties of the devices (Figure 1b). Additionally, energy dispersive X-ray spectrometry (EDX) elemental mappings (Figure S2a,b, Supporting Information) validate the detection of Fe and O signals within the anoxic FeO_x layer. The GQDs are discernible on the surface of the FeO_x layer, displaying the anticipated honeycomb-like graphene structures and hexagonal crystal arrangements (Figure 1bii–iv).^[19,20] Raman spectroscopy analysis reveals that the D, G, and 2D peaks are located at 1357, 1582, and 2680 cm^{-1} , respectively. The intensity ratio of the D band to the G peak (I_D/I_G) is measured at 0.93, and the broad, asymmetric nature of the 2D peak indicates the presence of defects and size variations in the GQDs (Figure 1c).^[21–23] For the electrical characterization, the GQDs-assisted devices underwent DC voltage sweeping, which unveiled a characteristic nonvolatile hysteresis curve, achieved without an electroforming step (Figure 1d). Under cyclic voltage sweeps, the negative current gradually increases while the positive current gradually decreases, resulting in an analog variation in conductance. The acquisition of analog conductance is crucial for achieving the biological weight regulation necessary for the development of artificial neural networks.^[23] The observed asymmetry in the I – V curves points to distinct dynamics of carrier migration during both the set and reset processes.

To elucidate the impact of GQDs, we performed a series of electrical tests on devices with varying concentrations of GQDs to assess the performance improvement achieved with increased concentrations of GQDs. Devices without or with low GQDs concentration (0.6 mg mL^{-1}) exhibited high switching voltages, unstable I – V curves, and the requirement of electroforming (Figure S3a,b, Supporting Information). Conversely, devices infused with higher concentrations of GQDs (1.2 and 1.8 mg mL^{-1}) displayed reduced switching voltages, stable I – V characteristics, and the absence of electroforming (Figure S3c, Supporting Information; Figure 1e). This improvement can be attributed to the localized electric field effects induced by GQDs, which effectively regulate the conductive pathways and modulate the interface barrier.^[21] Furthermore, the asymmetry ratio—calculated as the ratio of I_{set} to I_{reset} at a read voltage of $\pm 1 \text{ V}$ —exhibits a notable increase from 1.6 to 30. This finding suggests that the modulation of the interface by GQDs promotes asymmetric carrier movement. Therefore, increasing the concentration of GQDs appears to facilitate more efficient defect-assisted carrier transport (Figure 1e).^[24–26] However, as the concentration of GQDs increases to 2.4 mg mL^{-1} , the switching voltage of the GQDs-assisted devices increases, which may be attributed to the thick GQDs passivation layer obstructing the conductive path (Figure S3d, Supporting Information). The GQDs-assisted synaptic devices exhibited impressive retention and endurance, as evidenced by Figure S4 (Supporting Information), thereby affirming their reliability and efficacy for applications in neural networks, including data storage and information processing. To assess the uniformity and scalability potential of these GQDs-assisted devices, we engineered and characterized 6×6 array structures with GQDs concentrations of 1.2 and 1.8 mg mL^{-1} , as depicted in Figure S5a,d (Supporting Information), respectively. Further-

more, atomic force microscopy (AFM) analysis verified the uniform coating of GQDs on the device surface (Figure S6, Supporting Information). The mapping of the high-resistance state (HRS) and low-resistance state (LRS) for the array devices is illustrated in Figure S5b,c,e,f (Supporting Information), respectively. Statistical analysis of the resistance distribution indicates a relatively concentrated spread of resistance states. Collectively, these findings underscore the feasibility of the GQDs-assisted devices developed herein for large-scale array manufacturing.

2.2. GQDs-Assisted Synaptic Functions

Synaptic plasticity is a key mechanism facilitating the communication between adjacent neurons and serves as a biological foundation for learning and memory by regulating the strength and quantity of connections between neurons.^[27,28] Based on the characteristics of biological electric pulses and the operational voltage of the device in DC mode, we selected various pulse sequences to investigate the synaptic plasticity of GQDs-assisted devices. In principle, the GQDs-assisted device simulates the synaptic structure, wherein the bottom electrode acts as the presynaptic terminal for inputting presynaptic spikes, and the top electrode functions as the postsynaptic terminal for outputting postsynaptic current (Figure 2a). To investigate the alterations in synaptic device weight, we modulated the input pulse stimulation, as depicted in Figure 2b,c. Specifically, an enhancing pulse sequence comprising 50 pulses, each with a duration of 0.6 ms, was applied to the bottom electrode of the synaptic device. Notably, an amplitude of -1.2 V was sufficient to enhance the performance of the GQDs-assisted device; however, higher pulse amplitudes led to a steeper increase in conductance changes. Furthermore, when the same enhancing pulse sequence of 50 pulses with an amplitude of -1.2 V was applied to the bottom electrode of the GQDs-assisted device, a pulse width of 0.6 ms effectively enhanced the GQDs-assisted device, while longer pulse widths elicited even more significant variations in conductance.

Modulating the weight of the GQDs-assisted device is influenced by both the amplitude and duration of the applied pulses, which underscores the potential for input flexibility in regulating synaptic plasticity. Additionally, we examined the response of the device to a solitary presynaptic pulse, which demonstrated an increase in the excitatory postsynaptic current (EPSC) followed by a spontaneous decay within 60 ms. This behavior successfully emulated the short-term plasticity observed in biological synapses, as illustrated in Figure 2d. Moreover, the paired-pulse facilitation (PPF) function (Figure S7a,b, Supporting Information) revealed an exponential decay in weight change as the paired-pulse time interval (Δt) increased, which aligns with the characteristic forgetting behavior exhibited by biological synapses.^[29] Additional bio-inspired functionality such as STDP can be achieved using an overlapping pulse design, which is a fundamental mechanism governing the learning rules in biological neural networks.^[30] As depicted in Figure 2e, the performance of the GQDs-assisted device can either be enhanced ($\Delta t > 0$) or suppressed ($\Delta t < 0$), contingent upon the time interval (Δt) between the pre-synaptic and post-synaptic potentials. Notably, an increase in this interval results in a diminished effect, whether in enhancement or depression. These findings substantiate that GQDs-assisted

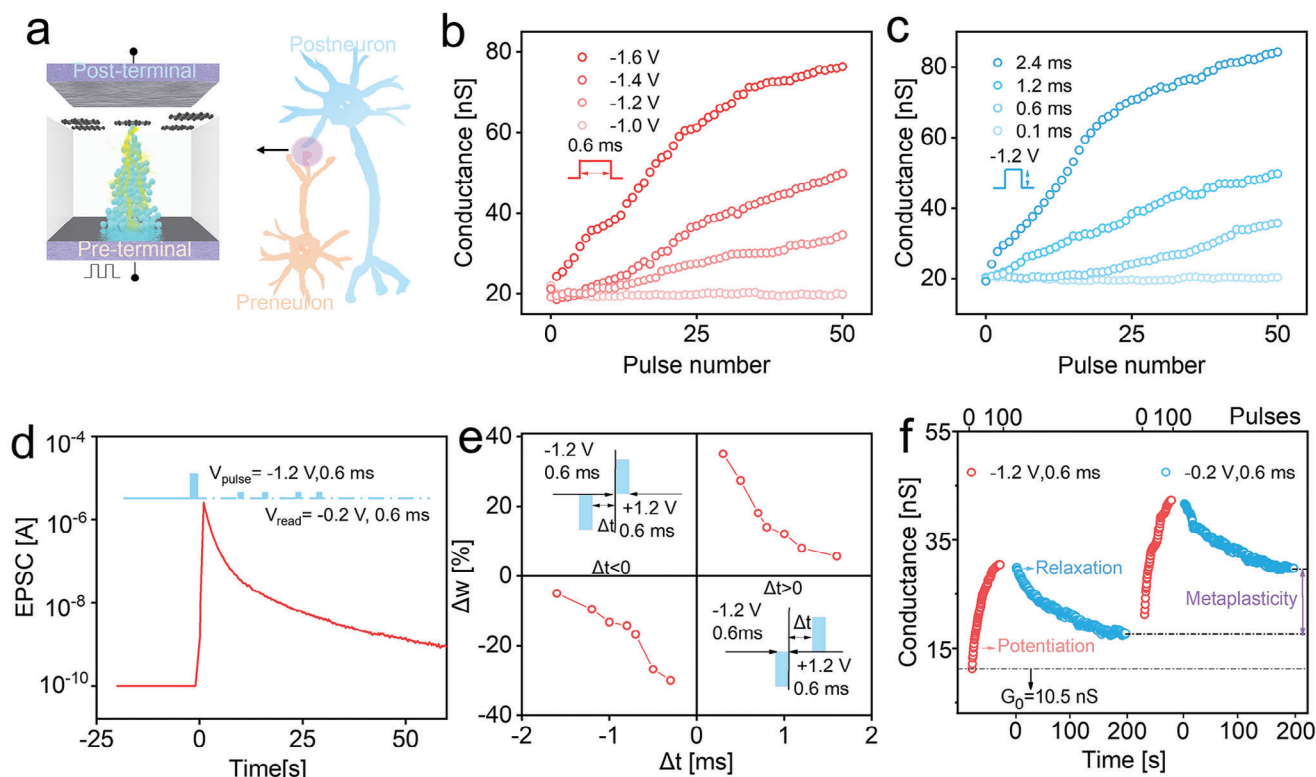


Figure 2. a) Schematic of the biological synapse (right) and artificial synapse (left). Synaptic weight as a function curve of the number of potentiation pulses at various b) pulse amplitudes and c) widths. d) Excitatory postsynaptic current (EPSC) characteristics of GQDs-assisted devices by a presynaptic spike (-1.2 V, 0.6 ms). e) Demonstration of STDP in GQDs-assisted devices. f) Metaplasticity is demonstrated after two potentiation processes. Initial conductance, $G_0 = 10.5$ nS.

devices adeptly replicate the fundamental plasticity characteristics of biological synapses, which is an essential aspect for improving learning and memory capabilities within neuromorphic networks.

To further elucidate the phenomenon of synaptic metaplasticity, a sequence of pulse trains was administered as postsynaptic spikes (Figure 2f). Following the application of 100 consecutive excitatory pulses, the GQDs-assisted device demonstrated a notable enhancement in synaptic weight, subsequently experiencing a spontaneous decay over a span of 200 s, which stabilized at an intermediate state of 23.4 nS ($>G_0$), indicative of long-term plasticity. Upon the re-application of an additional 100 consecutive excitatory pulses, a second decay was observed within the same 200 s timeframe, leading to a resting conductance value that was twice that of the initial decay. This observed behavior contrasts sharply with the typical conductance alterations associated with conventional artificial synaptic devices.^[31]

For instance, various studies involving FeO_x -based artificial synapses have primarily focused on simulating classical synaptic plasticity phenomena—such as long-term potentiation (LTP), short-term potentiation (STP), and spike-timing-dependent plasticity (STDP)—by manipulating different adaptive currents or interface barriers.^[32–35] For GQDs-assisted devices, the two enhanced pulse voltages can be regarded as two learning experiences, and the plasticity of the GQDs-assisted device is modulated according to the state of its historical plasticity—a phenomenon known as synaptic metaplasticity.^[36,37] This observa-

tion suggests that the GQDs-assisted device is capable of exhibiting both synaptic metaplasticity and plasticity, thereby showcasing its potential to replicate the intricate learning and memory processes inherent in biological neural networks.

2.3. Current Behavior of Metaplasticity and Switching Mechanism

Metaplasticity is a crucial concept in neuroscience that significantly influences synaptic plasticity, particularly through mechanisms such as facilitation of LTP (FLTP) and inhibition of LTP (ILTP).^[38,39] FLTP serves to enhance the efficacy of LTP, whereas ILTP prevents neuronal saturation by generating inhibitory signals that disrupt previously encoded memories (Figure S8, Supporting Information). This dynamic function addresses the challenges posed by Hebb's learning rule. In our research, we mimic this key metaplasticity phenomenon utilizing GQDs-assisted devices. This innovative approach enables neurons to achieve an excited and active state prior to the learning process, thereby enhancing their capacity for subsequent learning. By administering a series of positive and negative voltage pulses, we induce sustained enhancement and inhibition within synaptic devices, facilitating the exploration of two pivotal aspects of plasticity: FLTP and ILTP (Figure S9a–c, Supporting Information). The symmetric pulse sequence illustrated in Figure S9a (Supporting Information) reveals asymmetric weight changes, which

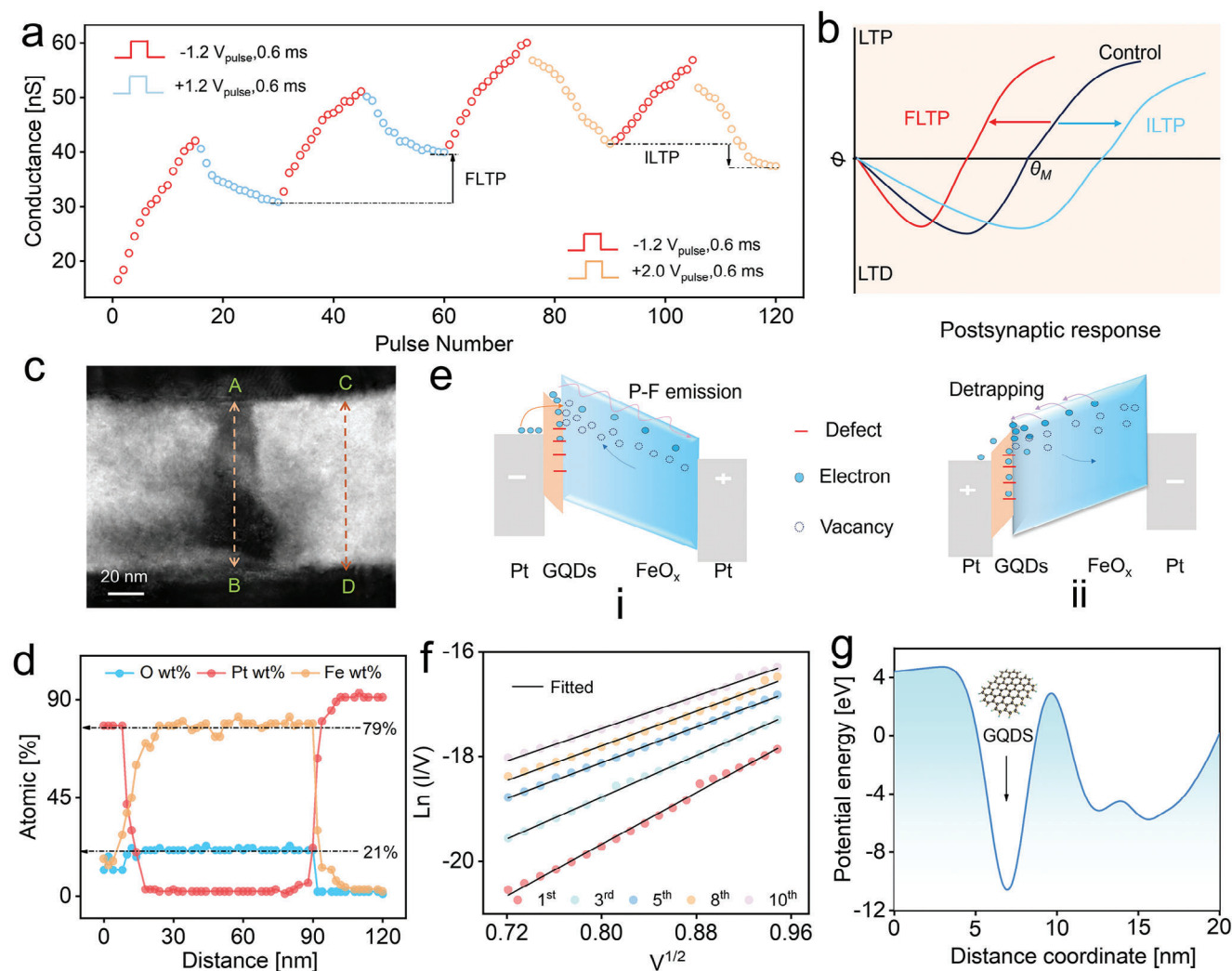


Figure 3. a) Metaplastic facilitation of long-term potentiation and the metaplastic inhibition of long-term potentiation. b) Biological metaplasticity curve. Vertical axis: weight correction amount ϕ ; horizontal axis: threshold level (θ) of postsynaptic discharge required for LTP generation by input stimuli. Black line (θ_M) as control. c) TEM image of the conductive pathway (CP). d) EDX profiles of Fe, O, and Pt at the line AB crossing the CP. e) Schematic of energy band during i) SET and ii) RESET processes. f) Part of the fitting results of the I - V curve of GQDs-assisted synaptic devices in Figure 1c SET: $\ln(I/V)$ versus $V^{1/2}$. g) Distribution of potential energy wells in FeO_x .

correspond with behaviors observed in Figure 1d. Furthermore, as depicted in Figure S9b,c (Supporting Information), upon reaching an equivalent potentiation state, an increase in the amplitude of the inhibitory pulse leads to tunable weight adjustments, causing the weight changes to symmetrically transition into an over-inhibitory state. This observation corroborates existing research indicating that the spatial and situational memory capabilities of the mammalian hippocampus are contingent upon environmental conditions.^[40]

This tunable methodology presents a promising potential for achieving multimodal and non-isomorphic computation in neuromorphic networks. Consequently, the variability in conductance is directly influenced by the amplitude of the inhibitory pulse. Next, inhibition pulse amplitudes of 1.2, 1.6, and 2 V are selected to simulate the modulation of memory weights by synaptic metaplasticity. GQDs-assisted artificial synapses demonstrate remarkable performance with delays reaching up to 63.2 and

71 μs under negative and positive pulse voltages, respectively (Figure S10, Supporting Information). This impressive capability provides a robust groundwork for the development of efficient, rapid, and bio-inspired neural networks, which are essential for a wide array of real-time and complex applications. Additionally, the conductance modulation exhibits commendable linearity (Figure S9d,e, Supporting Information), which is vital for the deployment of traditional training algorithms within neuromorphic computing frameworks.^[41]

To further substantiate the viability of history-dependent plasticity in memristors, we implemented continuous potentiation and inhibition pulse sequences, which consist of two distinct phases, as depicted in Figure 3a. In the initial phase, the postsynaptic weight (i.e., conductance) systematically increases following the application of two identical symmetric pulse sequences. In the subsequent phase, an asymmetric pulse sequence is introduced, which progressively reduces

the postsynaptic weight. This dual-phase process emulates the concept of historical experiences, wherein varying pulse sequences symbolize different learning encounters. The synaptic weight of GQDs-assisted devices is effectively modulated by these symmetric or asymmetric pulse sequences, thus facilitating history-dependent plasticity. The application of diverse amplitudes of inhibitory pulses plays a crucial role in determining the threshold level for long-term postsynaptic memory discharge (Figure 3b), which is similar to the glutamate-mediated synaptic plasticity mechanisms in the hippocampus.

The sliding threshold property is a fundamental attribute of neural networks, as it imparts stability and regulatory capacity. Specifically, the modulation of the plasticity induction threshold (θ_M) as a function of cumulative historical activities enables the network to adapt and regulate its synaptic plasticity. The dynamic modulation of the membrane potential (θ_M) significantly influences LTP. Specifically, an elevation in θ_M complicates the induction of LTP, whereas a reduction in θ_M promotes LTP, particularly when postsynaptic neuronal activity is minimal. The regulation of metaplasticity serves to lower the plasticity induction threshold for certain synaptic groups, thereby enhancing cognitive functions related to learning and memory. Although previous research has established that plasticity plays a role in regulating LTP, the foundation of neural network development relies on weight alterations being directly influenced by the interactions between presynaptic and postsynaptic neurons, thereby minimizing the impact of uncontrolled presynaptic stimulation.^[42,43] Furthermore, metaplasticity may also involve mechanisms related to LTD, indicating the need for additional investigation in this area.

To investigate the underlying mechanisms contributing to the resistive switching behavior of the developed GQDs-assisted devices, we employed transmission electron microscopy (TEM) to analyze ultrathin samples of these devices post-solidification. A significantly elevated electric field, surpassing the standard operating voltage, was applied (Figure S11, Supporting Information) to enhance our ability to observe the distribution and concentration of oxygen vacancies influenced by the locally intense electric field generated by the GQDs. This localized strong electric field is further illustrated in the accompanying simulation diagram (Figure S12, Supporting Information). Notably, as depicted in Figure 3c, we identified a dark region approximately 10 nm in diameter, which serves as a conduit between the upper and lower electrodes. To further confirm and analyze the chemical composition of the path in the dark region, we conducted an energy-dispersive X-ray (EDX) analysis. The distribution patterns of Pt, Fe, and O along the AB line, which intersects at CP, and the CD line, located outside of CP (Figure 3c,d; Figure S2b, Supporting Information), reveal that the oxygen concentration along line AB is significantly lower than that along line CD. This observation implies that the localized electric field is effective in concentrating oxygen vacancies around line AB. The presence of regularly distributed oxygen vacancies creates localized defect states that facilitate the capture and release of electrons, thereby promoting stable current flow. Furthermore, the ordered nature of these defect states minimizes randomness in the electron migration process, which

enhances the uniformity of electrical behavior, as supported by references.^[21,23,44,45]

In devices that do not incorporate GQDs, the injection of thermally activated electrons into the resistive layer encounters energy barriers, which correlates strongly with the Schottky emission mechanism (refer to Figure S13b,c, Supporting Information). The random dispersion of oxygen vacancies leads to the formation of erratic defect states for electron migration, resulting in elevated threshold voltage and an unstable hysteresis curve. Conversely, in GQDs-assisted artificial synaptic devices, as illustrated in Figure 3e–i, the defects within the GQDs effectively capture electrons that are injected from the electrodes. As the electric field intensifies, the electrons accumulated in the GQDs from the electrode gain sufficient kinetic energy to migrate to the defect energy levels (O vacancies) in the FeO_x layer through the P–F emission mechanism. This movement can be attributed to the strong local electric field that causes the aggregation of oxygen vacancies in the FeO_x layer, lowers its conduction band energy level, and provides a stable and accessible migration pathway for electrons, thereby achieving stable and repeatable switching behavior. This process can be reasonably fitted using P–F emission, as depicted in Figure 3f. The fitted slope demonstrates an increase with each application of voltage cycles (Table S1, Supporting Information), which signifies a gradual adaptation of the localized strong electric field around the O vacancy defects. This adjustment effectively lowers the interface barrier height, thereby increasing the likelihood of electron emission. As illustrated in Figure 3eii, when a symmetric positive bias is applied, electrons migrate along the electric field and are subsequently re-captured by defects within the GQDs, impeding further electron migration toward the electrode. Concurrently, this results in a disruption of the uniform distribution of oxygen vacancies, leading to an elevation in the conduction band energy level of FeO_x , which consequently induces a decline in device conductivity. This phenomenon is reflected in the asymmetric I – V curve depicted in Figure 1c.

Furthermore, Figure 3g illustrates the potential energy wells of FeO_x derived from first-principles calculations, which corroborate the localized accumulation of electrons. Upon reapplication of a negative bias, the electrons stored in the GQDs are released into the resistive switching layer, resulting in an increased current density and an associated rise in weight. A greater positive bias is subsequently necessary to facilitate the return of electrons from the GQDs to the electrodes for recombination, leading to a significant reduction in conductance. This reduction adversely impacts the subsequent enhancement of process weight formation. A comprehensive overview of the conductance modulation process is detailed in Figure S14 (Supporting Information). Therefore, the dependence of conductance on inhibition voltage successfully simulates the ability of biological synaptic metaplasticity to regulate plasticity.

2.4. Demonstration of Stable Neural Circuit Memory Rules Based on Synaptic Metaplasticity

In the intricate neural circuitry of the hippocampus, metaplasticity is instrumental in modulating local neural activity through the mechanisms of synaptic plasticity, facilitating dynamic

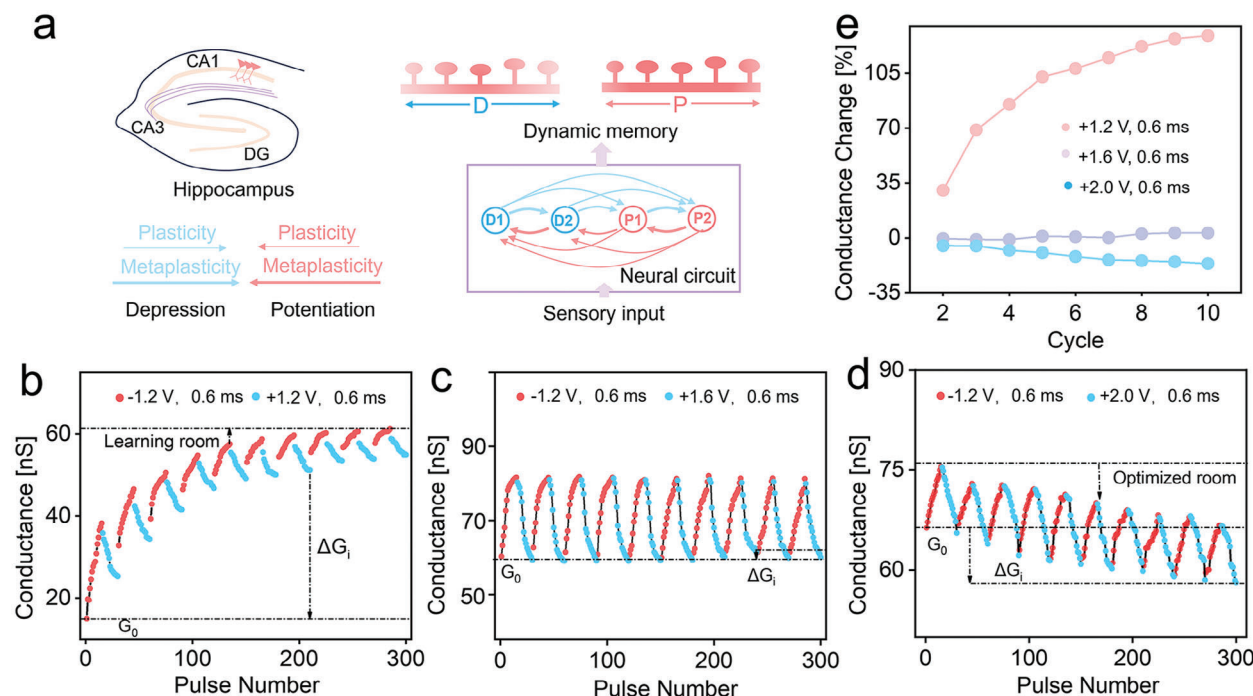


Figure 4. a) Neural circuits in the hippocampus region. Metaplasticity modulates the connectivity strength of synaptic groups, achieving a balance between memory stability and learning plasticity. Multiple adjustments of conductance based on metaplasticity. Perform conductance programming with 15 negative pulses/15 positive pulses for 10 cycles. Pulse conditions for testing: pulse width of 0.6 ms, negative pulse of -1.2 V, and positive pulse of b) $+1.2$ V; c) $+1.6$ V; d) $+2.0$ V. e) 10 cycles corresponding to conductance changes: $(\Delta G_i/G_0) \times 100\%$.

learning processes in response to central indicator signals.^[39] This phenomenon significantly enhances neuronal excitability in the CA1 region of the hippocampus, subsequently improving the capacity for learning in subsequent tasks and promoting the formation of additional synapses, which collectively strengthen memory retention (Figure 4a).^[46,47] Concurrently, metaplasticity fine-tunes the states of neural activity, thereby creating an adaptive learning environment suitable for a variety of learning tasks. To assess the repeatability of metaplasticity in regulating LTP behaviors, we employed diverse continuous pulse trains that represent various scenarios of learning and memory. Figure 4b–d depicts the processes of long-term enhancement and inhibition across 10 cycles. By leveraging the weight of historical memory, we observed modifications in the plasticity of re-memorization, which not only enhanced memory capabilities but also preserved learning space for the acquisition of new skills (Figure 4b).

Furthermore, when inhibitory stimuli were increased, synaptic devices demonstrated stable and invariant plasticity (Figure 4c), highlighting their strong repeatability and robustness. This finding suggests that synaptic devices also exhibit consistent changes in electrical conductance during conventional synaptic cycles, a critical characteristic of traditional neural networks. Additionally, by administering heightened inhibitory stimuli, multiple instances of ILTP were implemented to mitigate the risk of memory overload-induced impairment, thereby optimizing the availability of learning space for further cognitive tasks (Figure 4d). By adjusting the pulse trains,

the synaptic device achieves dynamic experience-based regulation of synaptic plasticity, which provides dynamic stability for maintaining effective neuronal output. In the biological brain, specific connections between excitatory and inhibitory neurons are achieved through mechanisms of plasticity, which ultimately form the fundamental core neural network module (Figure 4a). This module is responsible for encoding the memory state of the brain. Figure 4e depicts the dynamic changes in conductance of synaptic devices as they are modulated by varying memory states, corresponding to the details illustrated in Figures 4b–d. The observed changes in synaptic weight align with existing literature that suggests memory regulation within the hippocampus is significantly influenced by environmental factors, personal experiences, and the ontological state of the organism. This conductance alteration is indicative of shifts in memory efficiency and is intricately linked to pulse regulation, which is essential for the development of large-scale neural networks. Note that, despite the general consensus on the importance of metaplasticity in neuromorphic computing, there is a scarcity of literature that explores its practical application within network frameworks. Most research tends to focus on metaplasticity in isolation or extends its implications to LTP and LTD phenomena, without establishing a connection to broader network dynamics (Table S2, Supporting Information). Therefore, we emphasize the necessity of integrating artificial metaplastic synaptic devices directly into neural networks, as a means to mitigate the challenge of catastrophic forgetting.

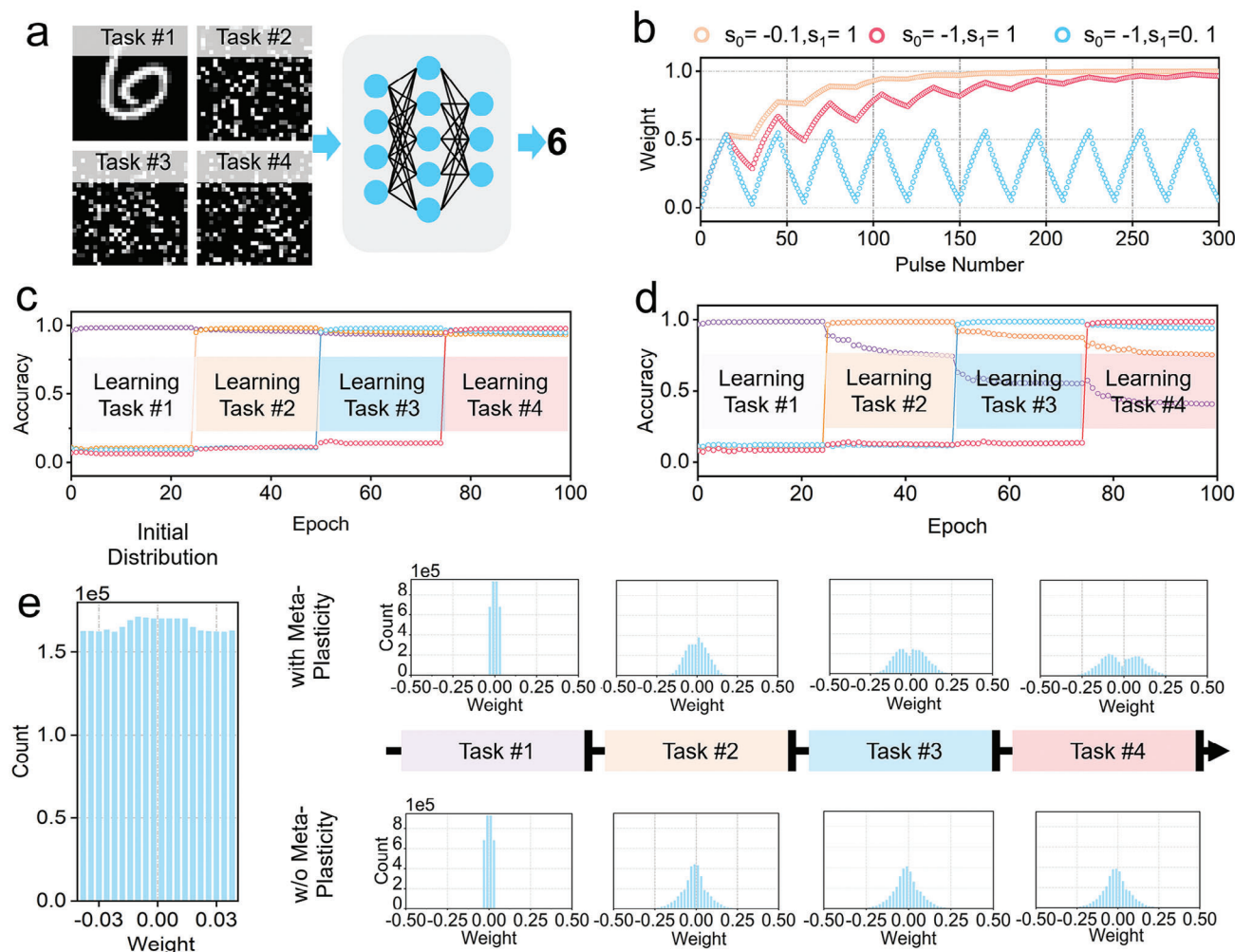


Figure 5. Effects of device metaplasticity on catastrophic forgetting problem. a) Continual learning permuted MNIST datasets with a $784 \times 4096 \times 10$ multiple-layer perceptron. Tasks #2, #3, and #4 are generated by randomly shuffling the pixels of the original MNIST images (Task #1) with fixed seeds. b) Examples of conductance trajectory simulated by (Equation 1) when applied negative and positive stimuli (15 pulses for each) sequentially for 10 cycles. All three curves have $\lambda_{\text{inc}} = \lambda_{\text{dec}} = 1$ and $w_{\text{max}} = 1$ but varying configurations of s_0, s_1 . c) Evaluation accuracy of 4 tasks when training the neural network with metaplasticity, which achieves higher accuracy of the previous and overall tasks compared to d) naive model. e) Evolution of weight distribution. We visualize the weight distribution at the initial and at the last epoch of training each task. Weights trained with metaplasticity conform to the hump-shaped distribution (first row) and weights directly trained via the Adam optimizer conform to the Gaussian distribution (second row).

2.5. Synaptic Metaplasticity Alleviates Catastrophic Forgetting in Neuromorphic Networks

The incorporation of synaptic metaplasticity into neuromorphic architectures signifies a pivotal advancement in reconciling the functionalities of neuromorphic networks with the sustained learning capabilities observed in biological systems. This integration is essential for developing strategies to counteract the issue of catastrophic forgetting in neuromorphic environments. This study demonstrates that GQDs-assisted devices with metaplasticity can mitigate the catastrophic forgetting problem of neuromorphic networks. Herein, we sequentially present four training sets to a fully connected neural network (Figure 5a). The metaplastic device serves as an innovative weight consolidation mechanism, where a negative stimulus triggers maximum conductance, whereas a positive stimulus inhibits con-

ductance, although not restoring it completely to its minimum value. This dynamic not only establishes a foundational conductance level but also mitigates weight decay throughout the learning process (Figure 5b). To assess the impact of metaplasticity, we employ a sequential permuted MNIST learning task (Figure 5c). The initial task involves the classification of the original MNIST dataset, followed by three additional tasks that require the classification of permuted MNIST datasets. Each task is executed over 25 training epochs. Remarkably, after completing all four consecutive tasks, the network achieves a learning accuracy of 97% and a memory accuracy of 94%. In stark contrast, the naive model attains high accuracy for the current task; however, it rapidly forgets the previously learned weight configurations, resulting in subpar performance on earlier tasks, as illustrated in Figure 5d. The model equipped with metaplasticity outperforms the naive approach, maintaining superior

accuracy on prior tasks. Both models utilize the Adam optimizer for weight updates; however, the metaplasticity-enabled model is additionally trained with L1 regularization, which promotes the development of a sparse weight matrix. Our intuition is that if the weights significant to the current task are sufficiently consolidated, they would hardly change conductance levels when learning new tasks. Moreover, we observed that weights approaching zero, or those that are entirely zero, are actively adjusted—either increased for positive weights or decreased for negative weights—to better accommodate new tasks. Notably, the weights of the model trained with meta-plasticity evolve into a hump-shaped distribution (Figure 5e, first row), in stark contrast to the naive model, which develops a Gaussian distribution (Figure 5e, second row). This achievement in metaplasticity within single synaptic hardware presents a pioneering approach for the realization of extensive, reconfigurable, dynamic learning neuromorphic networks. Such networks hold the promise of advancing energy-efficient artificial intelligence systems, diverging from traditional digital algorithm-based architectures.^[18,48,49]

3. Conclusion

This study elucidates a distinctive metaplastic synaptic behavior exhibited by two-terminal GQDs-assisted devices, which may provide a viable strategy to combat catastrophic forgetting in neural network hardware. The modification of the GQDs/FeO_x interface facilitates stable analog conductance alterations that replicate key synaptic plasticity phenomena, including STDP, PPF, and LTP, under a variety of pulse sequences. Significantly, the device demonstrates both FLTP and ILTP via pulse programming, thereby affirming its metaplastic synaptic characteristics. By employing specific pulse sequences, the GQDs-assisted synaptic device effectively emulates the dynamic outputs of neural circuits in a range of memory learning contexts. In a continuous learning assessment involving four distinct tasks, the device maintains an accuracy level exceeding 94% even after extended learning periods. This performance indicates a successful equilibrium between memory stability and learning plasticity, effectively mitigating the challenges associated with catastrophic forgetting. These GQDs-assisted synaptic devices exhibited significant potential in neural morphology computing, thereby bridging the gap between artificial intelligence and human brain intelligence.

4. Experimental Section

Device Fabrication: The fabrication process commenced with the selection of *p*-type heavily doped silicon wafers oriented in the (111) crystallographic direction, which served as the substrate. A 300-nm-thick layer of SiO₂ was first grown on these wafers. Subsequently, a 50-nm-thick Pt bottom electrode was meticulously patterned using standard photolithography techniques followed by DC magnetron sputtering. Following this, an insulating layer of silicon nitride (SiN_x) (60 nm) was deposited. This layer featured a via-hole structure with a diameter of 3 μm, created through another round of photolithography, and was subsequently sputtered using radio frequency (RF) magnetron sputtering. Subsequently, a 40-nm-thick layer of FeO_x, which serves as the resistive switching layer, was deposited within the via-holes via RF magnetron sputtering. To prepare the GQDs, a concentration of 1 mg mL⁻¹ was established by dispersing the GQDs in an isopropanol solution. The GQDs utilized in this research were procured from McLean Biochemical Co., Ltd. The GQDs solution was spin-coated

onto the surface of the FeO_x film at a rotation speed of 4000 rpm, ensuring a uniform distribution. To complete the device architecture, a final layer of Pt, also 40 nm in thickness, was deposited as the top electrode using DC magnetron sputtering.

Characterizations and Measurements: The morphological characteristics of the GQDs on the device surface were assessed using atomic force microscopy (AFM, XE70, Park Systems). The structural properties of the GQDs were analyzed through Raman spectroscopy utilizing a Via Raman Microscope (Renishaw). Furthermore, the cross-sectional analysis of the GQDs-assisted device samples was conducted using high-resolution transmission electron microscopy (HR-TEM, JEOL, JEM-3000F). At the outset, all devices were configured in a high-resistance state. The electrical measurements were conducted at room temperature under vacuum, using a Keithley 4200 semiconductor parameter analyzer and Cascade probe station with two modules: the 4200-SMU DC source unit with high-precision preamplifiers and the 4225-PMU waveform generator unit for pulse measurements. Initially, all devices were in a high-resistance state.

Silvaco TCAD Simulation Electric Field Distribution Test: To develop this model, a multilayer structure was initially established in ATLAS comprising a bottom Pt electrode, a layer of FeO_x, and a top Pt electrode. To assess the influence of the thickness of the FeO_x layer on device performance, its thickness was systematically reduced by half. Subsequently, GQDs of the smallest feasible size at were introduced the interface between the Pt and FeO_x layers to ensure their precise placement. To enhance the insulating characteristics of the GQDs—rendering them more effective insulators than FeO_x—the bandgap energy of the GQDs was elevated to 3.0 eV, surpassing the bandgap of FeO_x (≈2.4 eV). Furthermore, the effective density of states for both electrons and holes was minimized to 1 × 10¹⁷ cm⁻³ and the carrier mobilities were decreased to 1 cm² V⁻¹ s⁻¹. This reduction aimed to limit both the number and mobility of charge carriers, consequently lowering the electrical conductivity. To finalize the model, relevant physical models were implemented, including the Shockley–Read–Hall (SRH) recombination model, along with concentration-dependent and field-dependent mobility models. We established boundary conditions, such as electrode work functions and applied voltage biases, thereby rendering the model ready for simulation runs and subsequent analysis using TonyPlot.

Density Functional Theory Simulation Calculations: Spin-polarized density functional theory (DFT) calculations were performed using Vienna Ab Initio Simulation Package (VASP). The projection augmented wave (PAW) method and pseudopotential approach were instrumental in analyzing the valence state configurations for Fe and O atoms, characterized by *d*⁷*s*¹ and *s*²*p*⁴ configurations, respectively. Comprehensive structural optimizations were performed on each slab of Fe₂O₃, alongside their corresponding heterostructures. The calculations of the density of states for these heterostructures utilized a Monkhorst–Pack (MP) *k*-point mesh, specifically a grid of 5 × 3 × 1 points within the Brillouin zone. A plane wave basis set, accompanied by an energy cutoff of 530 eV, was employed to accurately represent the electron wave orbitals. The convergence criterion for electronic self-consistency was meticulously set to 10⁻⁷ eV, while the relaxation force convergence threshold was established at 0.005 eV Å⁻¹.

Simulation of Metaplastic Behavior to Alleviate Catastrophic Forgetting in Neuromorphic Networks: The metaplasticity behavior can be simulated using the following Equation (1):

$$\begin{aligned} f_{inc}(w) &= \lambda_{inc}(w_{max} - |w|) \\ f_{dec}(w) &= \lambda_{dec}|w_{base} - w| \\ w_{base} &= \left(s_0 + \max_{n=0,1,\dots} \{ |w_n| \} \cdot (s_1 - s_0) \right) \cdot \text{sign}(w) \\ w_{n+1} &= w_n + \begin{cases} f_{inc}(w_n) \cdot U_w, & \text{if } w_n \cdot U_w > 0, \\ f_{dec}(w_n) \cdot U_w, & \text{otherwise} \end{cases} \end{aligned} \quad (1)$$

where *w* denotes the weight, that is, the normalized conductance. *f*_{inc} and *f*_{dec} represent the window functions resulting nonlinearity and boundary, *λ*_{inc} and *λ*_{dec} determine the rate of convergence. *w*_{max} denotes the maximum value of normalized weight (*w*_{max} = 1 in this work). *w*_{base} refers to the basic conductance level which the synapse decays to when positive stimulus is applied. *s*₀ and *s*₁ represent the fitting parameters. *U*_w denotes

the weight update item of specific optimizer; for straightforward gradient descent algorithm, it is $-\alpha \cdot \Delta w$, where α denotes the learning rate and Δw indicates the gradient of loss with respect to weight. We considered f_{inc} if the weight update prescribes to increase $|w|$ otherwise f_{dec} .

The experimental data pertaining to LTP and LTD is intricately connected to the ongoing learning processes associated with the permuted MNIST dataset through a systematic approach. Initially, the derivative of GLTP with respect to the pulse index P was computed, as outlined in Equation (2) (where P is interpreted as a temporal variable):^[50]

$$\frac{dG_{LTP}}{dP} = \frac{B}{A} e^{-\frac{P}{A}} \quad (2)$$

Substituting Equation (2) into Equation (S7, Supporting Information) results in the formulation presented in Equation (3):

$$\frac{dG_{LTP}}{dP} = \frac{B + G_{min} - G_{LTP}}{A} \quad (3)$$

Significantly, Equation (3) eliminates any reliance on temporal factors or pulse indices, focusing exclusively on the existing conductance level. This aligns with the expression of the metaplastic learning rule, which takes a structurally analogous form. By designating U_w as the step size, Equation (4) can be derived:

$$\begin{cases} \lambda_{inc} = \frac{1}{A} \\ w_{max} = B + G_{min} \end{cases} \quad (4)$$

As the weight w in metaplastic learning rule represents the normalized conductance level (i.e., $G_{min} = 0$; $G_{max} = 1$), and P_{max}/A denotes a large value, $w_{max} \approx 1$. It can be concluded that Equation (4) bridges the metaplastic learning rule in continual learning with LTP/LTD data.

Supporting Information

Supporting Information is available from the Wiley Online Library or from the author.

Acknowledgements

This work was supported by the National Natural Science Foundation of China (Grants No.62204219) and the Major Program of Natural Science Foundation of Zhejiang Province (Grants No. LDT23F0401). The authors acknowledge Dr. Jiabao Sun of ZJU Micro-Nano Fabrication Center for his assistance during the magnetron sputtering. The authors would like to express sincere gratitude to Zixiang Zhang for creating the illustration used in this paper, and Yao Jiacheng for assisting with the first-principles simulation.

Conflict of Interest

The authors declare no conflict of interest.

Data Availability Statement

The data that support the findings of this study are available on request from the corresponding author. The data are not publicly available due to privacy or ethical restrictions.

Keywords

catastrophic forgetting, QODs, metaplasticity, synaptic devices

Received: July 31, 2024

Revised: November 6, 2024

Published online: December 8, 2024

- [1] D. Silver, A. Huang, C. J. Maddison, A. Guez, L. Sifre, G. Van Den Driessche, D. Hassabis, *Nature* **2016**, 529, 484.
- [2] G. St-Yves, E. J. Allen, Y. Wu, K. Kay, T. Naselaris, *Nat. Commun.* **2023**, 14, 3329.
- [3] P. Kłosowski, *IEEE, SPA* **2018**, 223–228.
- [4] T. T. adros, G. P. Krishnan, R. Ramyaa, M. Bazhenov, *Nat. Commun.* **2022**, 13, 7742.
- [5] I. Munoz-Martin, S. Bianchi, G. Pedretti, O. Melnic, S. Ambrogio, D. Ielmini, *IEEE JXCD* **2019**, 5, 58.
- [6] X. Zhang, C. Zhong, J. Zhang, T. Wang, W. W. Ng, *Neurocomputing* **2023**, 526, 143.
- [7] J. Tang, F. Yuan, X. Shen, Z. Wang, M. Rao, Y. He, H. Wu, *Adv. Mater.* **2019**, 31, 1902761.
- [8] G. Dellaferriera, S. Woźniak, G. Indiveri, A. Pantazi, E. Eleftheriou, *Nat. Commun.* **2022**, 13, 1885.
- [9] F. Ferrini, J. Perez-Sanchez, S. Ferland, L. E. Lorenzo, A. G. Godin, I. Plasencia-Fernandez, C. Salio, *Nat. Commun.* **2022**, 11, 3935.
- [10] D. Shi, W. Wang, Y. Liang, L. Duan, G. Du, *Nano Lett.* **2023**, 23, 11662.
- [11] M. U. Khan, C. M. Furqan, J. Kim, S. A. Khan, Q. M. Saqib, M. Y. Chougale, H. S. Kwok, *ACS Appl. Electron.* **2022**, 4, 297.
- [12] C. Lu, J. Meng, J. Song, T. Wang, H. Zhu, Q. Q. Sun, L. Chen, *Nano Lett.* **2024**, 24, 1667.
- [13] Z. H. Tan, R. Yang, K. Terabe, X. B. Yin, X. D. Zhang, X. Guo, *Adv. Mater.* **2015**, 28, 377.
- [14] X. Zhu, C. Du, Y. Jeong, W. D. Lu, *Nanoscale* **2017**, 7, 45.
- [15] T. H. Lee, H. G. Hwang, J. U. Woo, D. H. Kim, T. W. Kim, S. Nahm, *ACS Appl. Mater. Interfaces* **2018**, 10, 25673.
- [16] D. Kireev, S. Liu, C. H. Bennett, D. Akinwande, J. A. C. Incorvia, *Nat. Commun.* **2022**, 13, 4386.
- [17] L. Danial, E. Pikhay, E. Herbelin, N. Wainstein, V. Gupta, N. Wald, S. Kvatinisky, *Nat. Electron* **2019**, 2, 596.
- [18] A. Laborieux, M. Ernout, T. Hirtzlin, D. Querlioz, *Nat. Commun.* **2021**, 12, 2549.
- [19] T. Zhang, W. Li, K. Huang, H. Guo, Z. Li, Y. Fang, J. Wu, *Nat. Commun.* **2021**, 12, 5265.
- [20] R. Ye, C. S. Xiang, J. Lin, Z. W. Peng, K. W. G. Huang, Z. Yan, N. P. Cook, E. L. G. Samuel, C. C. Hwang, G. Ruan, G. Ceriotti, A. R. Raji, A. A. Martí, J. M. Tour, *Nat. Commun.* **2013**, 4, 2943.
- [21] C. H. Wang, W. He, Y. S. Zhang, K. J. Huang, R. Zhao, *Small* **2017**, 13, 1603435.
- [22] F. Liu, M. Jang, H. D. Ha, *Adv. Mater.* **2013**, 25, 3657.
- [23] V. R. Nallagatla, H. G. Kim, D. Yoo, G. Yi, M. Kim, C. U. Jung, *Adv. Electron. Mater.* **2023**, 9, 2300401.
- [24] J. Huang, S. Yang, X. Tang, L. Yang, W. Chen, Z. Chen, X. Li, Z. Zeng, Z. Tang, X. Gui, *Adv. Mater.* **2023**, 35, 2303737.
- [25] V. K. Sangwan, H. S. Lee, H. Bergeron, I. Balla, M. E. Beck, K. S. Chen, M. C. Hersam, *Nature* **2018**, 554, 500.
- [26] A. M. Van Der Zande, P. Y. Huang, D. A. Chenet, T. C. Berkelbach, Y. You, G. H. Lee, J. C. Hone, *Nature Mater.* **2013**, 12, 554.
- [27] G. Shen, C. Zhuge, J. Jiang, Y. Fu, Y. Zheng, Z. Qin, D. He, *Adv. Funct. Mater.* **2023**, 34, 2309054.
- [28] B. Lyu, Y. Choi, H. Jing, C. Qian, H. Kang, S. Lee, J. H. Cho, *Adv. Mater.* **2020**, 2, 1907633.
- [29] Y. Wang, Y. G. Zheng, E. Li, X. Lian, W. Chen, *InfoMat* **2021**, 3, 917.
- [30] W. Huh, D. Lee, C. H. Lee, *Adv. Mater.* **2020**, 32, 2002092.
- [31] P. Chen, F. Liu, P. Lin, *Nat. Commun.* **2023**, 14, 6184.
- [32] C. Liao, X. Hu, X. Liu, B. Sun, *Appl. Phys. Lett.* **2022**, 121, 123505.
- [33] G. Zhou, X. Y. Ji, J. Li, F. Zhou, Z. Dong, B. Yan, B. Sun, W. Wang, X. Hu, Q. Song, L. Wang, S. Duan, *IScience* **2022**, 25, 105240.
- [34] C. Wang, R. Zhao, *Sci. Rep.* **2016**, 6, 22970.
- [35] X. Wan, F. Gao, X. Lian, X. Ji, E. Hu, L. He, Y. Tong, Y. Guo, *Jpn. J. Appl. Phys.* **2018**, 57, 060303.

- [36] R. A. John, F. Liu, N. A. Chien, M. R. Kulkarni, C. Zhu, Q. Fu, A. Basu, Z. Liu, N. Mathews, *Adv. Mater.* **2018**, *30*, 1800220.
- [37] Y. M. Fu, H. Li, L. Huang, T. Wei, F. Hidayati, A. Song, *Adv. Electron. Mater.* **2022**, *8*, 2200463.
- [38] C. Wickliffe, Abraham, F. Mark, *Trends Neurosci.* **1996**, *19*, 126.
- [39] A. P. Crestani, J. N. Krueger, E. V. Barragan, Y. Nakazawa, S. E. Nemes, J. A. Quillfeldt, B. J. Wiltgen, *Neuropsychopharmacol.* **2019**, *44*, 408.
- [40] T. Zhang, X. Cheng, S. Jia, C. T. Li, M. M. Poo, B. Xu, *Sci. Adv.* **2023**, *9*, 2947.
- [41] H. Zhang, B. Jiang, C. Cheng, B. Huang, H. Zhang, R. Chen, F. Zhou, *Nano Lett.* **2023**, *23*, 3107.
- [42] L. Luo, *Science* **2021**, *373*, 7285.
- [43] C. Schmidt-Hieber, P. Jonas, B. Jischofberger, *Nature* **2004**, *429*, 184.
- [44] X. Yan, Y. Pei, H. Chen, J. Zhao, Z. Zhou, H. Wang, L. Zhang, J. Wang, X. Li, C. Qin, G. Wang, Z. Xiao, Q. Zhao, K. Wang, H. Li, D. Ren, Q. Liu, H. Zhou, J. Chen, P. Zhou, *Adv. Mater.* **2019**, *31*, 1805284.
- [45] X. Yan, L. Zhang, H. Chen, X. Li, J. Wang, Q. Liu, C. Lu, J. Chen, H. Wu, P. Zhou, *Adv. Funct. Mater.* **2018**, *28*, 1803728.
- [46] S. Choi, J. Shin, G. Park, J. S. Eo, J. Jang, J. J. Yang, G. Wang, *Nat. Commun.* **2024**, *6*, 2044.
- [47] P. Yger, M. Gilson, *Front. Comput. Neurosci.* **2015**, *9*, 138.
- [48] P. Khorsand, A. Soltani, *PLoS Comput. Biol.* **2017**, *13*, e1005630.
- [49] F. T. Zohora, V. Karia, A. R. Daram, A. M. Zyarah, D. Kudithipudi, *2021 IEEE International Symposium on Circuits and Systems (ISCAS)*, IEEE, Daegu, Korea, **2021**, pp. 1–5.
- [50] X. Sun, S. Yu, *IEEE J. EM. SEL. TOP. C.* **2019**, *9*, 570.